49th AIAA Aerospace Sciences Meeting including the New Horizons Forum and Aerospace Exposition
4 - 7 January 2011, Orlando, Florida

AIAA 2011-736

Effects of Surface Roughness on Laminar Separation Bubble over a Wing at a Low-Reynolds Number

Ying Zhou[1] and Z.J. Wang[2]
Department of Aerospace Engineering and CFD Center, Iowa State University, Ames, IA 50011

Laminar separation bubbles (LSBs) are often found over the wing of micro air vehicles (MAV) at low Reynolds numbers, and strongly influence the lift, drag and other aerodynamic performance parameters. A numerical investigation of a passive LSB control techniques by using roughness bumps on a low-Reynolds number wing is conducted in this paper. A high-order spectral difference unstructured grid Navier-Stokes solver is employed in the simulations. The study of surface roughness on laminar separation and turbulent transition can provide insights into the design of future passive control devices on wings. The transitional flow with LSB past a SD7003 rectangular wing with Reynolds number of 60,000 is used as the basic (uncontrolled) case. In the controlled cases, roughness bumps are strategically located near the leading edge of the wing for the purpose of improving aerodynamic performance. The location, bump size, the number of bumps and the angle-of-attacke (AoA) are varied to study the effects. The pressure drag forces in the controlled cases are found to be reduced when the LSB are diminished or avoided, resulting in much improved lift over drag ratio

I. Introduction

Flow control, the technique to manipulate a flow field to achieve a desired change, is of immense technological importance, and thus is pursued by scientists and engineers in various areas of fluid mechanics field for many years. Low-Reynolds number ($Re_c = 10^4 \sim 10^5$) flow has been of interest for decades with the development of Micro Air Vehicles (MAV). In the low-Reynolds number flow over airfoils, the formation of a LSB may have a dominant effect on the flow field. In this paper, a passive flow control technique using surface roughness (bumps) near the leading-edge of the wing is numerically studied. The roughness bumps can affect the formation of the LSBs and for the purpose of aerodynamic performance improvement. The flow over the SD7003 wing at a AoA of 4 deg, Reynolds number $Re = 6 \times 10^4$ and Mach number $M = 0.2$ is used as the basic model and a starting point for the controlled models.

In the basic model, the laminar flow detaches from the suction wing surface near the leading edge and a 'long' type separation bubble is formed. Thereafter, the separated laminar boundary layer rapidly transitions to turbulence and the turbulent boundary layer reattaches after the vortex breakdown. Since laminar boundary layers are less resistible to the significant adverse pressure gradient, LSBs are widely found over the suction side of low-Reynolds-number airfoils at moderate incidences. The LSBs are usually regarded to cause the dramatic increase of drag force and the deterioration of the lifting surface performance. Flow control is aimed at improving the performance. By introducing the surface roughness (bumps) in this paper, the laminar boundary layers are severely perturbed or become turbulent, and thus are more resistible to the adverse pressure gradient. In such a way, the LSBs can be diminished and thus the wing regains the aerodynamic performance.

High-order methods on unstructured grids are known for their advantages of accuracy and flexibility in the numerical simulation of multi-scale flow with complex geometries. In the last two decades, there have been intensive research efforts on high-order methods for unstructured grids[1-13]. In this paper, a high-order SD method for the three dimensional Navier-Stokes equations on unstructured hexahedral grids developed by Sun et al.[13] is used. This approach is capable of capturing the laminar separation and the vortex breakdown, and has been previously shown in the numerical simulation of the attached/detached laminar flow and the reattached turbulent flow in the case of the basic model[14]. With the flexibility of unstructured grid to complex geometry in this method, the shape of

[1] Ph.D. Candidate, Dept. of Aerospace Engineering, 0245 Howe Hall, ying@iastate.edu, AIAA student member.
[2] Professor of Aerospace Engineering, 2271 Howe Hall, zjw@iastate.edu, Associate Fellow of AIAA.

the leading-edge bump can be modeled in the computational mesh without any assumption or additional equations.

The rest of the paper is organized as follows. In the next section, the numerical method is briefly reviewed. In section III, numerical results of the basic model are presented and the flow features associated with LSB are discussed. In section IV, a series of cases with different bump size, bump number and AoA are numerical simulated. The numerical results of the controlled cases are compared with those of the basic model and the detail effects of the surface roughness are investigated. Concluding remarks are given in section V.

II. Review of Multidomain Spectral Difference (SD) Method

Governing equations

Consider the three-dimensional compressible non-linear Navier-Stokes equations written in the conservation form as

$$\frac{\partial Q}{\partial t}+\frac{\partial F}{\partial x}+\frac{\partial G}{\partial y}+\frac{\partial H}{\partial z}=0 \tag{2.1a}$$

on domain $\Omega \times [0,T]$ and $\Omega \subset R^3$ with the initial condition

$$Q(x,y,z,0)=Q_0(x,y,z) \tag{2.1b}$$

and appropriate boundary conditions on $\partial\Omega$. In (2.1), x, y, and z are the Cartesian coordinates and $(x,y,z) \in \Omega$, $t \in [0,T]$ denotes time. Q is the vector of conserved variables, and F, G and H are the fluxes in the x, y and z directions, respectively.

Coordinate transformation

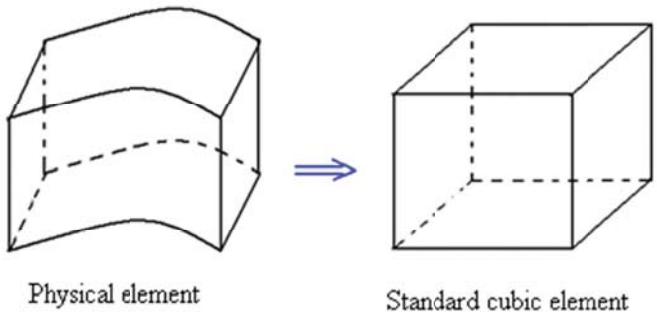

Figure 1. Transformation from a physical element to a standard element

In the SD method, it is assumed that the computational domain is divided into non-overlapping unstructured hexahedral cells or elements. In order to handle curved boundaries, both linear and quadratic isoparametric elements are employed, with linear elements used in the interior domain and quadratic elements used near high-order curved boundaries. In order to achieve an efficient implementation, all physical elements (x,y,z) are transformed into standard cubic element $(\xi,\eta,\varsigma) \in [-1,1] \times [-1,1] \times [-1,1]$ as shown in Figure 1.

The transformation can be written as

$$\begin{bmatrix} x \\ y \\ z \end{bmatrix}=\sum_{i=1}^{K} M_i(\xi,\eta,\varsigma)\begin{bmatrix} x_i \\ y_i \\ z_i \end{bmatrix} \tag{2.2}$$

where K is the number of points used to define the physical element, (x_i,y_i,z_i) are the Cartesian coordinates of these points, and $M_i(\xi,\eta,\varsigma)$ are the shape functions. For the transformation given in (2.2), the Jacobian matrix J takes the following form

$$J = \frac{\partial(x,y,z)}{\partial(\xi,\eta,\varsigma)} = \begin{bmatrix} x_\xi & x_\eta & x_\varsigma \\ y_\xi & y_\eta & y_\varsigma \\ z_\xi & z_\eta & z_\varsigma \end{bmatrix}.$$

The governing equations in the physical domain are then transformed into the standard element, and the transformed equations take the following form

$$\frac{\partial \tilde{Q}}{\partial t} + \frac{\partial \tilde{F}}{\partial \xi} + \frac{\partial \tilde{G}}{\partial \eta} + \frac{\partial \tilde{H}}{\partial \varsigma} = 0 \tag{2.3}$$

where

$$\tilde{Q} = |J| \cdot Q$$

$$\begin{bmatrix} \tilde{F} \\ \tilde{G} \\ \tilde{H} \end{bmatrix} = |J| \begin{bmatrix} \xi_x & \xi_y & \xi_z \\ \eta_x & \eta_y & \eta_z \\ \varsigma_x & \varsigma_y & \varsigma_z \end{bmatrix} \cdot \begin{bmatrix} F \\ G \\ H \end{bmatrix}$$

Spatial Discretization

In the standard element, two sets of points are defined, namely the solution points and the flux points, illustrated in Figure 2 for a 2D element. The solution unknowns (conserved variables Q) or degrees-of-freedoms (DOFs) are stored at the solution points, while fluxes are computed at the flux points. The solution points in 1D are chosen to be the Gauss points defined by

$$X_s = cos\left(\frac{2s-1}{2N} \cdot \pi\right), s = 1,2,\cdots,N. \tag{2.4}$$

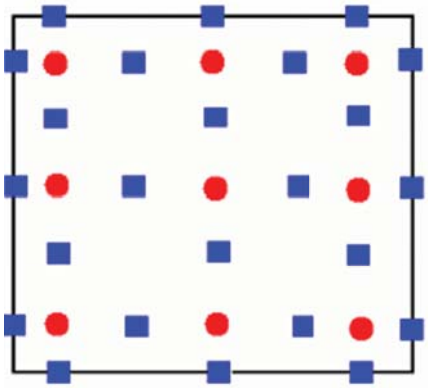

Figure 2. Distribution of solution points (circles) and flux points (squares) in a standard element for a 3rd-order SD scheme.

With solutions at N points, we can construct a degree $(N-1)$ polynomial in each coordinate direction using the following Lagrange basis defined as

$$h_i(X) = \prod_{s=1, s\neq i}^{N} \left(\frac{X - X_s}{X_i - X_s}\right) \tag{2.5}$$

The reconstructed solution for the conserved variables in the standard element is just the tensor products of the three one-dimensional polynomials, i.e.,

$$Q(\xi,\eta,\varsigma) = \sum_{k=1}^{N}\sum_{j=1}^{N}\sum_{i=1}^{N} \frac{\tilde{Q}_{i,j,k}}{|J_{i,j,k}|} h_i(\xi) \cdot h_j(\eta) \cdot h_k(\varsigma) \tag{2.6}$$

The flux points in 1D are chosen to be the $(N-1)$ Gauss quadrature points plus the two ending points. With fluxes at $(N+1)$ points, a degree N polynomial can be constructed in each coordinate direction using the following Lagrange bases defined as

$$l_{i+1/2}(X) = \prod_{s=0, s\neq i}^{N} \left(\frac{X - X_{s+1/2}}{X_{i+1/2} - X_{s+1/2}} \right) \tag{2.7}$$

Similarly, the reconstructed flux polynomials take the following form:

$$\tilde{F}(\xi,\eta,\varsigma) = \sum_{k=1}^{N}\sum_{j=1}^{N}\sum_{i=0}^{N} \tilde{F}_{i+1/2,j,k}\, l_{i+1/2}(\xi)\cdot h_j(\eta)\cdot h_k(\varsigma) \tag{2.8a}$$

$$\tilde{G}(\xi,\eta,\varsigma) = \sum_{k=1}^{N}\sum_{j=0}^{N}\sum_{i=1}^{N} \tilde{G}_{i,j+1/2,k}\, h_i(\xi)\cdot l_{j+1/2}(\eta)\cdot h_k(\varsigma) \tag{2.8b}$$

$$\tilde{H}(\xi,\eta,\varsigma) = \sum_{k=0}^{N}\sum_{j=1}^{N}\sum_{i=1}^{N} \tilde{H}_{i,j,k+1/2}\, h_i(\xi)\cdot h_j(\eta)\cdot l_{k+1/2}(\varsigma) \tag{2.8c}$$

Because the SD method is based on the differential form of the governing equations, the implementation is straightforward even for high-order curved boundaries. All the operations are basically one-dimensional in each coordinate direction and each coordinate direction shares the collocated solution points with others, resulting in improved efficiency. In summary, the algorithm to compute the inviscid flux and viscous flux and update the unknowns (DOFs) consists the following steps:

1. Given the conserved variables $\{Q_{i,j,k}\}$ at the solution points, compute the conserved variables $\{Q_{i+1/2,j,k}\}$ at the flux points using polynomial (2.6).
2. Note that inviscid flux is a function of the conserved solution and the viscous flux is a function of both the conserved solution and its gradient, taking flux $\tilde{F}$ for example:
$$\begin{cases} \tilde{F} = \tilde{F}^i - \tilde{F}^v \\ \tilde{F}^i_{i+1/2,j,k} = \tilde{F}^i\left(Q_{i+1/2,j,k}\right) \\ \tilde{F}^v_{i+1/2,j,k} = \tilde{F}^v\left(Q_{i+1/2,j,k}, \nabla Q_{i+1/2,j,k}\right) \end{cases} \tag{2.9}$$
Compute the inviscid fluxes $\{\tilde{F}^i_{i+1/2,j,k}\}$ at the interior flux points using the solution $\{Q_{i+1/2,j,k}\}$ computed at Step 1. Compute the viscous fluxes $\{\tilde{F}^v_{i+1/2,j,k}\}$ using the solution $\{Q_{i+1/2,j,k}\}$ computed at Step 1 and the gradient of the solutions $\{\nabla Q_{i+1/2,j,k}\}$ computed based on $\{Q_{i+1/2,j,k}\}$.
3. Compute the common inviscid flux at element interfaces using a Riemann solver (2.11), such as the Roe solver [15] and Russanov solver [13].
$$\tilde{F}^i = \tilde{F}^i(Q_L, Q_R) \tag{2.11}$$
where Q_L and Q_R represent the solutions from the two elements beside the interface.
Compute the common viscous flux at element interfaces using a viscous approach (2.12), such as the averaged approach and DG-like approach [13].
$$\tilde{F}^v = \tilde{F}^v(Q_L, Q_R, \nabla Q_L, \nabla Q_R) \tag{2.12}$$
Then compute the derivatives of the fluxes at all the solution points by using (2.13).
$$\left(\frac{\partial \tilde{F}}{\partial \xi}\right)_{i,j,k} = \sum_{r=0}^{N} \tilde{F}_{r+1/2,j,k}\, l'_{r+1/2}(\xi_i) \tag{2.13a}$$
$$\left(\frac{\partial \tilde{G}}{\partial \eta}\right)_{i,j,k} = \sum_{r=0}^{N} \tilde{G}_{i,r+1/2,k}\, l'_{r+1/2}(\eta_j) \tag{2.13b}$$
$$\left(\frac{\partial \tilde{H}}{\partial \varsigma}\right)_{i,j,k} = \sum_{r=0}^{N} \tilde{H}_{i,j,r+1/2}\, l'_{r+1/2}(\varsigma_k) \tag{2.13c}$$
4. Update the DOFs using a multistage TVD scheme for time integration of (2.14).

$$\frac{\partial \tilde{Q}_{i,j,k}}{\partial t} = -\left(\frac{\partial \tilde{F}}{\partial \xi} + \frac{\partial \tilde{G}}{\partial \eta} + \frac{\partial \tilde{H}}{\partial \varsigma}\right)_{i,j,k} \tag{2.14}$$

For more details about SD method on hexahedral mesh, the readers can refer to [13].

III. Basic Model

The basic model is numerically simulated first and then the results will be used to compare with and assess the controlled models. The computational grid and boundary condition are introduced below, and then the numerical results and the features associated with the LSB and turbulent transition are presented. In this paper, the cases with different model are named according to the AoA, w/ or w/o bumps and the additional bump parameters, e.g. 'AoA_4c' represents the controlled case at AoA $4deg$ and 'AoA_4' refers to the current case of the basic model.

Computational grid and boundary condition

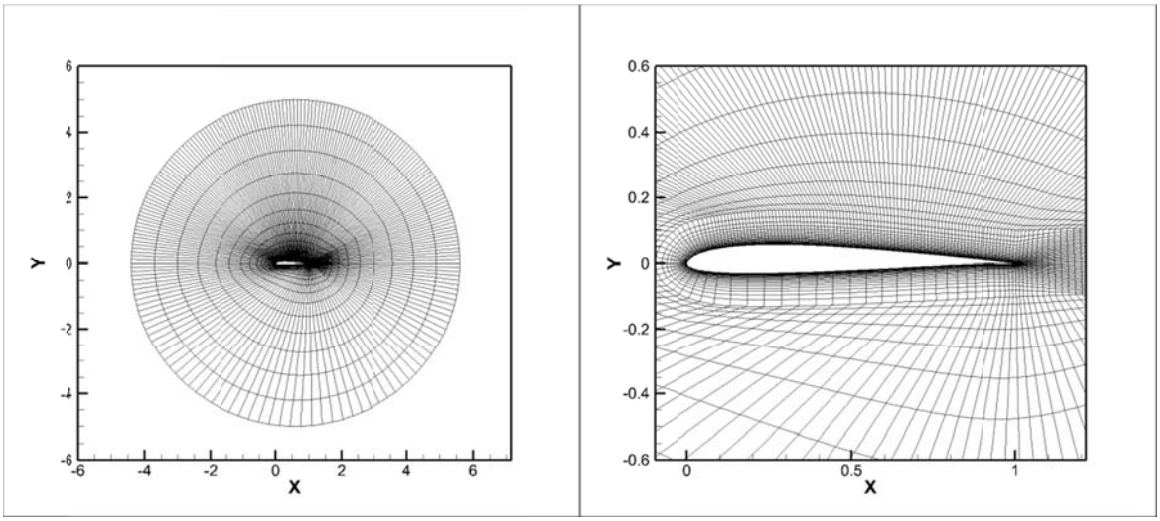

Figure 3. Computational mesh

Figure 3 shows the computational grid for the case AoA_4. Refined mesh is designed to concentrate finer elements near the wall and around the physically important region where the separation bubble and vortex breakdown occur. The smallest cells are located at the trailing edge corners with dimension (in wall units) $\Delta y^+ = 2.5$ in the direction normal to the wall, $\Delta x^+ = 25.0$ along the chord and $\Delta z^+ = 12.0$ in the spanwise direction. The total number of elements used here is 253,600, resulting in 6,847,200 and 16,230,400 degree-of-freedom (per equation) for 3rd-order and 4th-order SD method respectively. In the SD method, each cell is further discretized by the solution/flux points, so the resolution of the current mesh is close to what is required of a direct numerical simulation.

To model an infinite-span wing, a periodic boundary condition is used in the spanwise direction and the span width of the wing is set to be 20% of the chord, which was shown to be wide enough in [14&16]. At the far-field of the computational domain, an absorbing sponge zone boundary condition[17] is imposed. And a non-slip, adiabatic boundary condition is applied on the surface of the wing.

Averaged and statistical results

The numerical simulations are carried out at a Reynolds number based on the airfoil chord of $Re = 6 \times 10^4$ and Mach number $M = 0.2$. The AoA is $4\,deg$ in the current case. In Figure 4, the mean pressure coefficient $C_p = (p - p_\infty)/\frac{1}{2}\rho_\infty U_\infty^2$ and the mean skin friction coefficient $C_f = \tau/\frac{1}{2}\rho_\infty U_\infty^2$ distributions on the wing surface are shown. A polynomial order (p) refinement study is carried out by increasing the order of the polynomial in each element from 2 (resulting in 3rd-order accuracy) to 3 (resulting in 4th-order accuracy). A very good agreement between the 3rd-order method and 4th-order method has been found in Figure 4 for both the mean pressure coefficient and mean skin friction coefficient on the wing surface, thus indicating that the converged mean flow has been achieved and the spatial resolution provided by SD method is capable to capture the main flow features at this

Reynolds number. In the present study, the mean flow field and the statistical results are obtained by averaging the instantaneous flow field over 8 non-dimensional time $t = t^*/(c/U_\infty)$ units.

Table 1 compares the locations of separation, transition and reattachment between the 3rd-order and the 4th-order results. The onset location of transition is defined by a critical value of 0.001 of the normalized Reynolds stress as used in [18-21]. The differences between the above measurements of the 3rd-order and the 4th-order results are all less than 2%. The results from Galbraith et al.[16] are also listed here and the agreement here is also good.

Table 1. Separation, transition and reattachment locations

Case	Separation	Transition	Reattachment
3rd-order	0.223	0.515	0.675
4th-order	0.227	0.521	0.685
Galbraith et al. [16]	0.23	0.55	0.65

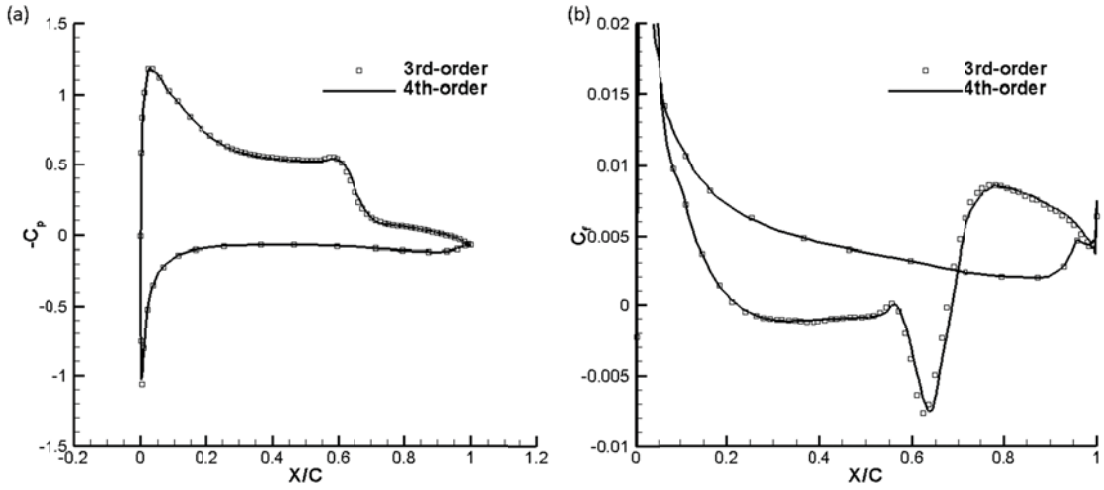

Figure 4. Mean pressure coefficient (left) and mean skin friction coefficient (right) on the wing surface. Square symbols: 3rd-order result; solid line: 4th-order result.

Flow features associated with LSB and turbulent transition

Figure 5a shows the mean streamlines around the wing and the mean streamwise velocity field averaged in both time and spanwise direction. The mean separation bubble and the reattachment of the flow are clearly shown. In Figure 5b, the low value of the mean spanwise vorticity on the suction surface of the wing at interval $x = [0.0,0.6]$ represents the laminar shear layer before the flow transitions into turbulent flow. The amplitude of the disturbance during this interval has been found to grow exponentially due to the Kelvin-Helmholtz instability after separation [14, 19-21]. The shear layer ends around $x = 0.65$ at the end of the LSB (Figure 5a) where the vortex breakdown occurs. A turbulent boundary layer forms at interval $x = [0.75,1.0]$. Figure 5c and d show the statistical distribution of the normalized turbulent kinetic energy $\left(T.K.E. = \frac{1}{2}\left(\overline{u'^2} + \overline{v'^2} + \overline{w'^2}\right)\right)$ and the normalized Reynolds stress $\left(\tau_{xy} = -\overline{u'v'}/U_\infty^2\right)$, respectively. The concentration of both the normalized $T.K.E.$ and Reynolds stress around $x \approx 0.65$ is strongly related to the process of vortex breakdown, and is discussed later in this section.

Figure 6 shows the profiles of the mean tangential velocity at different locations and the corresponding profiles of RMS tangential velocity disturbances at the corresponding locations of the basic model. Profiles are extruded in the wall's normal direction at each chord location. The development of the mean shear layer from an attached layer to a

detached one can be clearly seen. The profiles of RMS of u_t' vary along with the mean shear layer. After separation, the inflection point gradually shows in the mean velocity profiles (Figure 6.a) and the Kelvin-Helmholtz (K-H) instability becomes dominant and accompanies with vortex shedding.

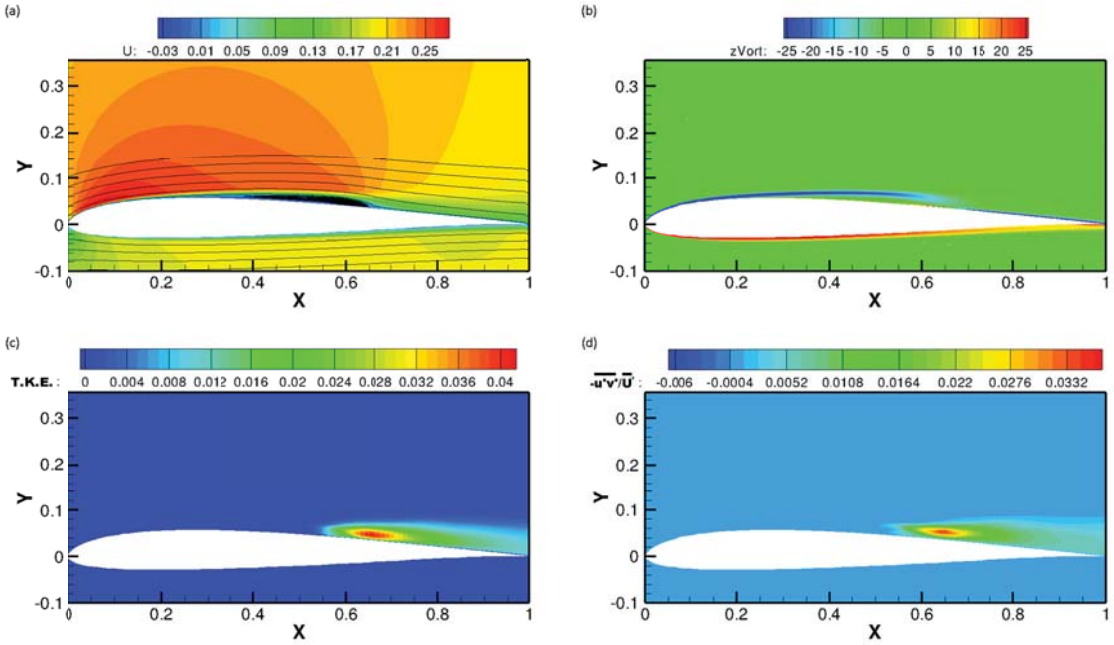

Figure 5. Mean and statistical results of basic model: (a) mean streamlines around the wing and mean streamwise velocity field; (b) mean spanwise vorticity field; (c) normalized turbulent kinetic energy ($T.K.E.$) distribution; (d) normalized Reynolds stress (τ_{xy}) distribution.

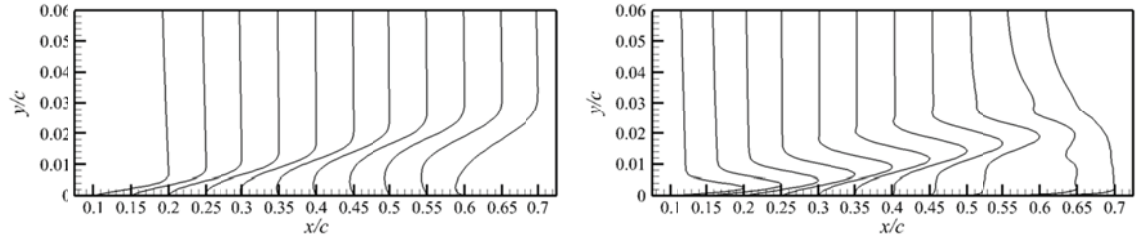

Figure 6 Numerical results for basic model: (a) normalized profiles of the mean tangential velocity at different locations; (b) normalized profiles of RMS tangential velocity disturbances at different locations

Figure 7 shows the instantaneous contour lines of the Q-invariant[30] for about a shedding period. Inside the detached shear layer (Figure 5b), vortical tubes (rolls) are shed and grow convectively, as shown in Figure 7. The K-H instability is also called inviscid instability, in which the disturbance has been found to be always more unstable in two dimensions than in three dimensions. The shedding vortex keeps the two-dimensional feature unstill entering the breakdown stage.

It is observed that two-dimensional vortices break down to small scale structures rapidly at interval $x = [0.6, 0.7]$, as shown in Figure 7. And in the same region, the skin friction and the wall pressure increase suddenly (Figure 4). Finally the flow reattaches to the wall and the LSB is closed by turbulent flow. It is observed in Figure 6 that the vortex breakdown process extends from the bottom to the top and the small scale structures close to the wall at interval $x = [0.6, 0.7]$ with upstream-going velocity play an important role in this process. A layer of small scale structures stay near the wall in this region right below the shedding vortices. As the layer remains inside the separation bubble, the small scale structures move upstream due to the reversed flow direction. When the shedding vortices pass the region, the bottom part of the shedding vortices meets and interacts with the upstream going small scale structures. The bottom part of the vortices breaks down to small scale structures first, then the upper part is affected and breaks down by the swirling motion of the vortices. In this way, the vortex tube breaks down from the

bottom to the top due to a feedback machnism[14]. After the breakdown of the large scale vortices into smaller scale eddies, the flow becomes more and more turbulent and propagates downstream. Spalart et al.[22] concluded this process as a simple mechanism of 'transition by contact'. Jones et al.[23] attributed a similar process to be caused by the three dimensional absolute instability.

The contours of the mean total pressure $P_{Total} = \frac{1}{2}\rho U^2 + P$ normalized by $\frac{1}{2}\rho_\infty U_\infty^2$, the mean pressure coefficient C_p distribution and the pressure gradient magnitude $|\nabla P|$ for the case AoA_4 are shown in Figure 8. Both the total pressure and the static pressure are almost constant inside the LSB region and are lower inside the LSB than those outside the LSB. In other words, in the average sense the LSB persists a constant low pressure inside and is pressed by high-pressure outside. Around the location $x \approx 0.65$, there exists a region of high adverse-pressure-gradient (APG) as shown in Figure 7c and a high pressure gradient terminates the LSB. This region around $x = 0.65$ is exactly the same region where the breakdown and reattachment are observed. In the sense of the mean flow field, it experiences the upstream low pressure and the downstream high pressure. To balance the pressure difference, the friction force increases over the wall as shown in Figure 4. The TKE and Reynolds stress are also found to be concentrated in the same region as shown in Figure 5c&d. The above features illustrate that this region is physically important to the formation of the LSB and the breakdown process thereafter, to which the attention should be paid when investigating the effects of the surface roughness.

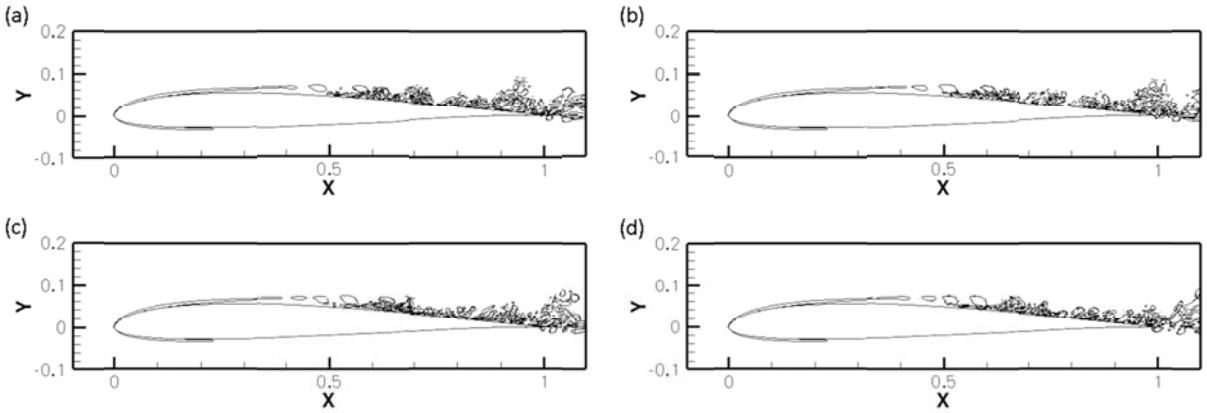

Figure 7. Instantaneous contour line of $Q = 1$ for about one shedding period

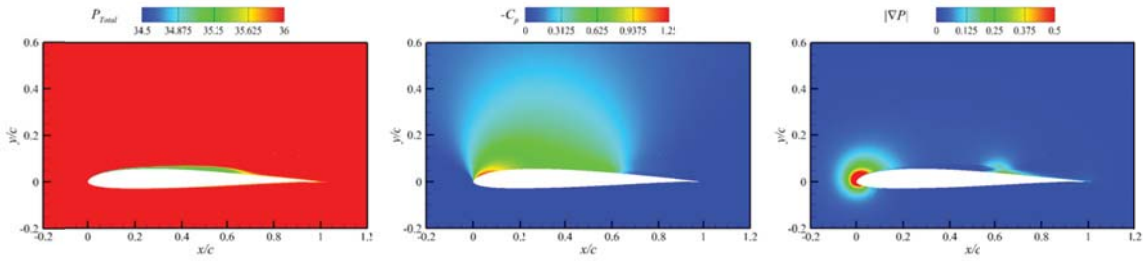

Figure 8. Averaged numerical results of case AoA_4: Contours of (a) normalized total pressure P_{Total}; (b) pressure coefficient $-C_p$; (c) pressure gradient magnitude $|\nabla P|$.

IV. Effects of Surface Roughness

In this section, the effects of the surface roughness on the separation and transition over the suction surface are investigated and discussed. The study may help improve the design of future passive control devices on the wing surface for separation reduction and transition control. Active flow control techniques have been widely adopted for the separation and transition control of flow over airfoils. Periodic air suction/blowing through a slot on the airfoil surface might be the most popular means of active control. With properly chosen frequency and magnitude of the suction/blowing speed, the technique is often found to be effective in reducing the separation region and improving performance. However, active control techniques such as suction/blowing usually require additional devices and is

less applicable to the separation control over a MAV wing, which should be light. The passive means of flow control involves 'inert' devices including changes to the wing shape and surface finish. Saric et al. [24, 25] pioneered the use of surface roughness as a means of passive flow control in their experimental studies. White and Saric[26] examined roughness effects on transition and found that three-dimensional static roughness can be an effective tool in delaying the transition to turbulence on a swept wing. Fransson et al.[28, 29] applied roughness elements on a flat plate in the wind-tunnel and found using this passive control technique they can delay transition to turbulence. Using numerical simulations, Honsaker and Huebsch[27] used a Prandtl transposition to model the surface roughness on airfoils and found that the dynamic surface roughness is effective on the stall separation control.

A passive flow control technique using roughness bumps is adopted here. By using the high-order SD method on unstructured hexahedral mesh, the shape and geometry of the roughness bump can be modeled as shown in Figure 9. The geometry of the roughness bump can be determined using the following parameters, the width W_{AC}, the length L_{BD} and the height H_{EF} of the bump. The surface edges of the bump are tangentially rejoined with the wing surface by high-order polynomial curves and the curved surface on the top (at point F) of the bump is also designed to be tangential to the original wing surface at point E, Figure 5. The location of the bump X_E and the number of bumps N_{bump} are also critical to the physics of the bump-induced disturbances and therefore the separation control effectiveness. And in all cases here, the bumps are equally spaced near the leading edge before the flow separates. Several cases with different geometries, numbers of bumps and AoAs are considered and numerically investigated here, and the parameters are listed in Table 2, 4 and 7. All the geometric parameters are normalized by the chord length c.

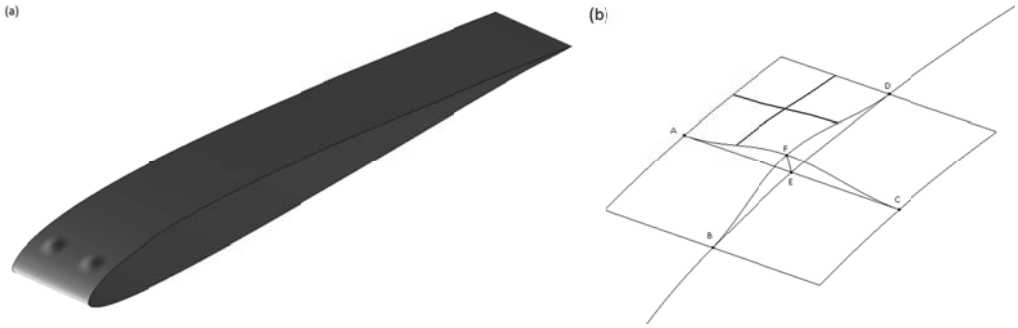

Figure 9. (a) Roughness bump on the wing surface and (b) bump geometries

Effects of bump size

Three controlled cases are simulated in this section to test the effects of the bump size. Through trial and error, the bump size and height were found to affect the flow more than the bump location. Here in all cases, the bumps are placed at $x = 0.05$, where the boundary layer thickness for the basic model AoA_4 is $\delta_E = 0.0049$. The geometric parameters of the roughness bumps in all three cases are shown in Table 2. The location and dimension of the bumps in AoA_4c are chosen after a few tests, in order to affect the attached boundary layer profile before separation and also not induce too much viscous drag force. The cases AoA_4c.w and AoA_4c.h are variations of AoA_4c. Comparing with AoA_4c, the bumps in AoA_4c.w are wider and the bumps in AoA_4c.h are taller, with the rest of the parameters being the same. The bumps in AoA_4c.w are twice as wide (W_{AC}) as in AoA_4c. In cases AoA_4c and AoA_4c.w, the height of the bumps is about 70% of the boundary layer thickness δ_E, while in case AoA_4c.h the height is equal to δ_E.

The instantaneous iso-surfaces and side-views of the Q-invariant in the cases of basic model and three controlled models are shown in Figure 10. The effectiveness of the bumps in changing the flow field of the basic model can be clearly seen. In case AoA_4c, vortex shedding in the separation bubble region is observed as in the basic model AoA_4. However the shedding vortices are distorted as streamwise vorticity is generated behind the bumps. The shedding vortices are closer to the airfoil surface and the frequency of vortex shedding is higher than that in the basic model, as shown in Figure 10b. It is found in both AoA_4c.w and AoA_4c.h that small scale vortex packets are generated behind the bumps and the pattern is periodic (Figure 10c&d). This implies that changing the width and height of the bumps can dramatically change the flow features, and the wider and taller bumps introduce stronger disturbances and significantly affect the laminar boundary layer flow. The perturbed region (periodic

vortical packets) after the bumps grows in the flow direction, takes over the laminar region. Eventually the boundary layer becomes fully turbulent as shown in Figure 10c&d. Vortex shedding (rolls) is also found in the laminar region of the flow, and the interaction with adjacent periodic vortical packets is observed. In these cases, the roughness bumps act like turbulators.

Table 2. Parameters of the roughness bumps

Case	X_E	W_{AC}	L_{BD}	H_{EF}	N_{bump}	δ_E
AoA_4	N/A	N/A	N/A	N/A	N/A	0.0049
AoA_4c	0.05	0.045	0.045	0.0035	2	N/A
AoA_4c.w	0.05	0.090	0.045	0.0035	2	N/A
AoA_4c.h	0.05	0.045	0.045	0.005	2	N/A

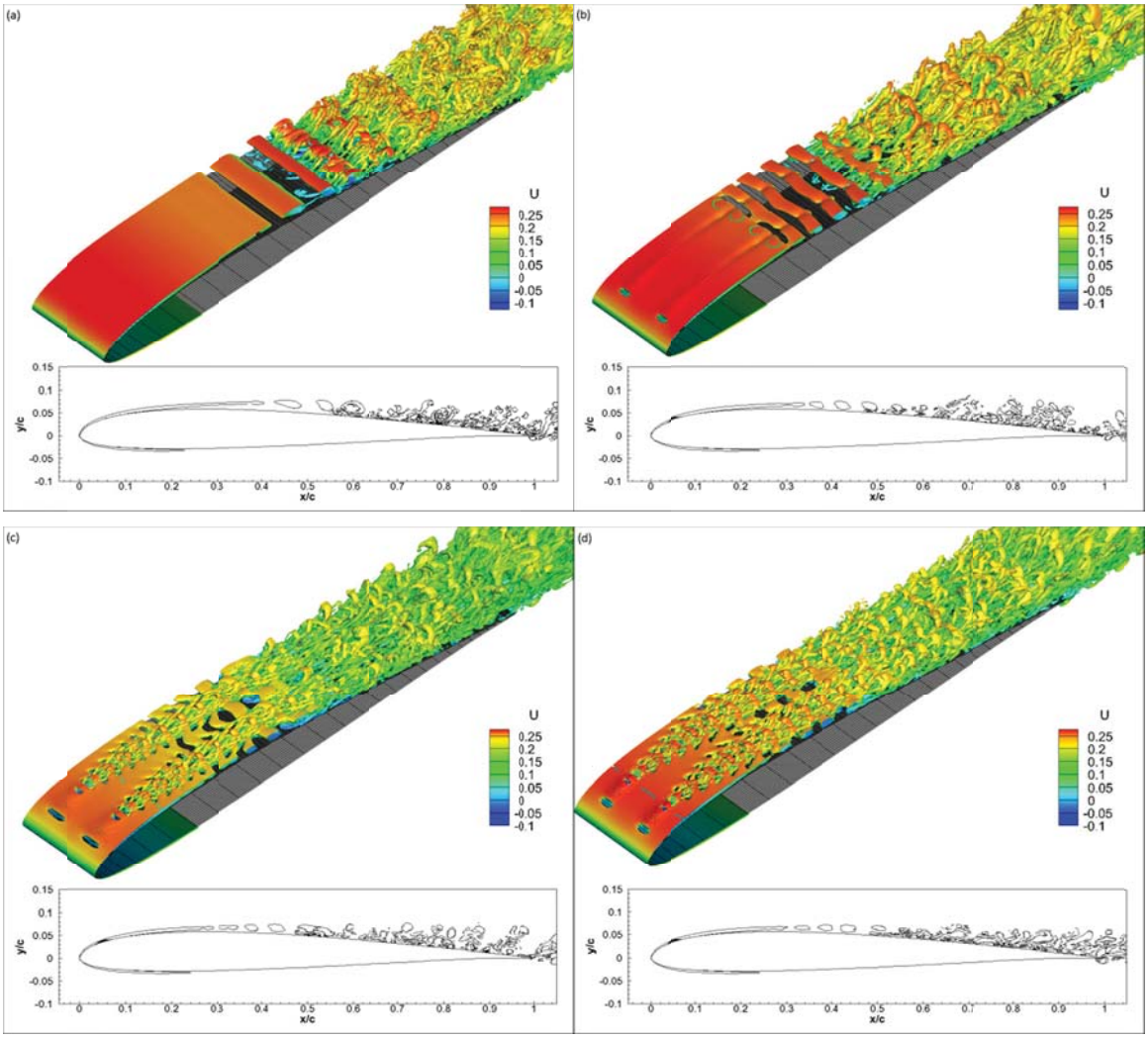

Figure 10. Iso-surface of $Q = 1$ colored by streamwise velocity and side-view of $Q = 1$; (a) AoA_4, (b) AoA_4c, (c) AoA_4c.w, (d) AoA_4c.h

The mean pressure coefficient and friction coefficient distributions on the suction surface of the controlled cases are shown in Figure 11, and compared with the results of the basic model. As shown in the friction coefficient plots, the separation region is smaller in case AoA_4c than in the basic model. Disturbed by the upstream bumps, flow separation is delayed, while the breakdown and reattachment occur at an earlier location. In case AoA_4c, the features associated with the LSB, which include a pressure plateau and steep pressure recovery at the strong separation region, are also observed. This indicates the flow characteristics in AoA_4c are quite similar to those in AoA_4, the basic model even though the flow field is disturbed by the streamwise vorticity generated by the bumps. The LSBs almost disappear in cases AoA_4c.w and AoA_4c.h as shown in Figure 11 in the friction coefficient plot. Without the separation region, the pressure recovers smoothly (Figure 11). The breakdown process is triggered by the vertical packets generated by the bumps, as shown in Figure 10c & d. Figure 12 shows the contours of the pressure gradient magnitude for cases AoA_4c and AoA_4c.h. Note that with a diminished LSB in case AoA_4c, the severe APG near $x = [0.5, 0.6]$ still shows up similar to case AoA_4. In case AoA_4c.h, however, the LSB is avoided and the severe APG region $x = [0.5, 0.6]$ disappears.

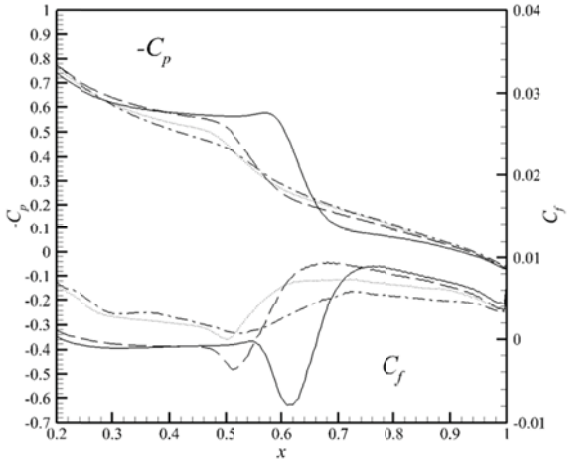

Figure 11. Mean pressure coefficient and mean skin friction coefficient on the wing surface; AoA_4 (solid line, ----), AoA_4c (dash line, - - -), AoA_4c.w (dash-dot line, -.-.-) and AoA_4c.h (dot line, ….)

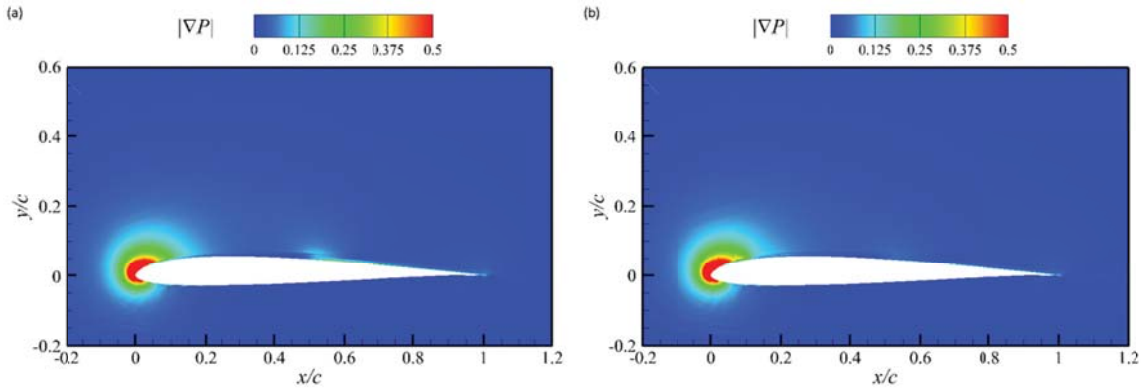

Figure 12. Contours of pressure gradient magnitude. (a) AoA_4c; (b)AoA_4c.h

Table 3 presents the mean lift and drag coefficients per unit span and the lift-to-drag ratio of all three cases. The drag coefficients decrease for all the controlled cases, and the lift coefficients also decrease slightly with the diminishing of the separation bubble. It can be seen by the flow field in Figure 10 and the friction coefficient in Figure 11, introducing the bumps results in more turbulent region and thus the friction induced drag increases. The contributions to the drag force C_D from both pressure drag C_{Dp} and friction drag C_{Df} are also listed in Table 3 for all the cases. It is shown that with the diminishing of the bubble, the pressure drag C_{Dp} decreases and the friction drag C_{Df} increases. However, the pressure drag decreases faster than the friction drag increases, and thus gain about 10% improvement of the lift-to-drag ratio for all the controlled cases, as shown in Table 3. Although the pressure drag C_{Dp} in AoA_4.w and AoA_4.h is lower than that in AoA_4, the friction drag C_{Df} is higher in these two cases due the

larger turbulent flow region. Thus AoA_4.c gives better lift-to-drag ratio than AoA_4.w and AoA_4.h.

Table 3. Mean lift coefficient, drag coefficient (per unit span) and lift-to-drag ratio

Case	C_L	C_D	C_{Dp}	C_{Df}	L/D
AoA_4	0.600	2.34e-2	1.38e-2	0.97e-2	25.6
AoA_4c	0.593	2.05e-2	1.00e-2	1.05e-2	28.9
AoA_4c.w	0.579	2.10e-2	0.94e-2	1.16e-2	27.6
AoA_4c.h	0.579	2.07e-2	0.95e-2	1.12e-2	28.0

Effect of the number of bump

In this part, the effects of the number of the bump are tested and investigated. Starting from case AoA_4c, AoA_4c.n keeps the other bump parameters the same, but reduces the bump width W_{AC} 50% and increases the number of bumps from 2 to 4. The detailed parameters of the roughness bumps can be found in Table 4. Figure 13 shows the instantaneous iso-surface and side-view of Q-invariant of case AoA_4c.n. For comparison, the same results of case AoA_4c are shown in Figure 10.b. Similar to case AoA_4c, the attached boundary layer and the following shedding vortices are perturbed but still remain laminar. Figure 14 shows the instantaneous contours of u-velocity and streamwise vorticity on the sliced plane at $y = 0.065$ for both cases AoA_4c and AoA_4c.n. The spanwise influences of the bumps on the laminar flow field and the development of the streamwise vorticity in the separation region can be clearly seen.

Table 4. Parameters of the roughness bumps

Case	X_E	W_{AC}	L_{BD}	H_{EF}	N_{bump}	δ_E
AoA_4c.n	0.10	0.0225	0.045	0.0035	4	N/A

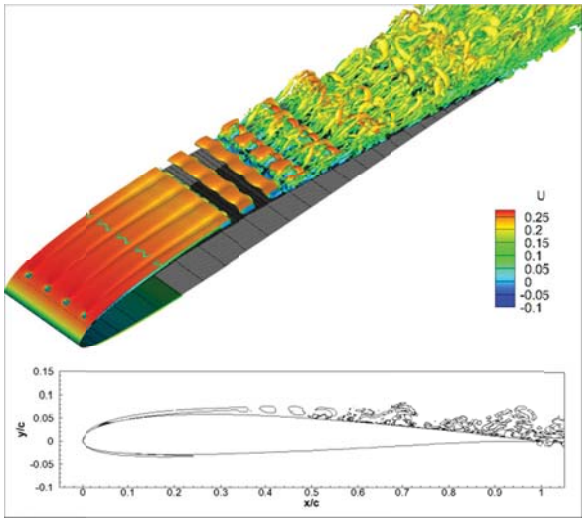

Figure 13. Iso-surface and side-view of $Q = 1$ colored by streamwise velocity of case AoA_4c.n

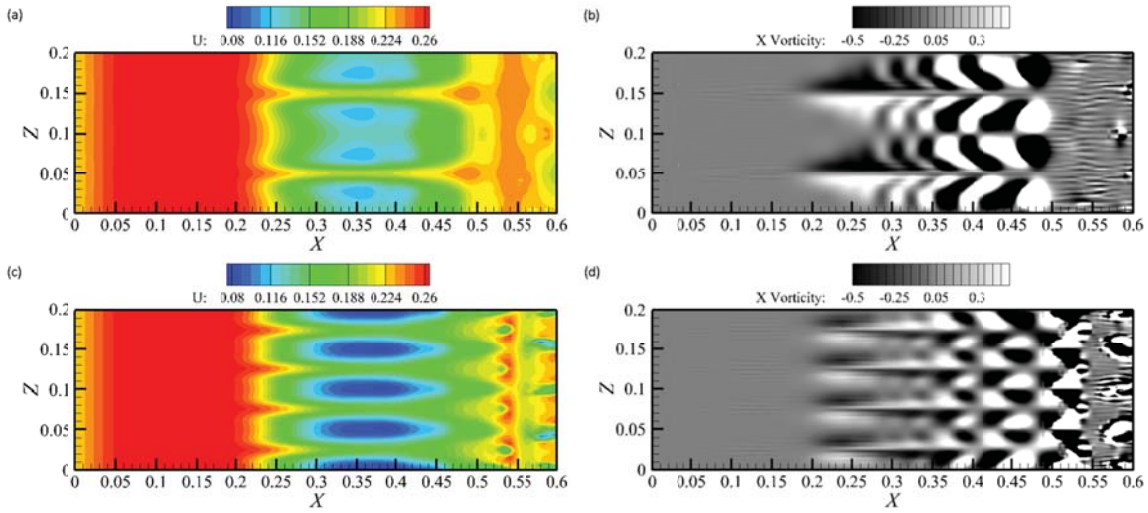

Figure 14. The instantaneous contours of u-velocity (left) and streamwise vorticity (right) on the sliced plane at $y = 0.065$; (upper) AoA_4c and (lower) AoA_4c.n

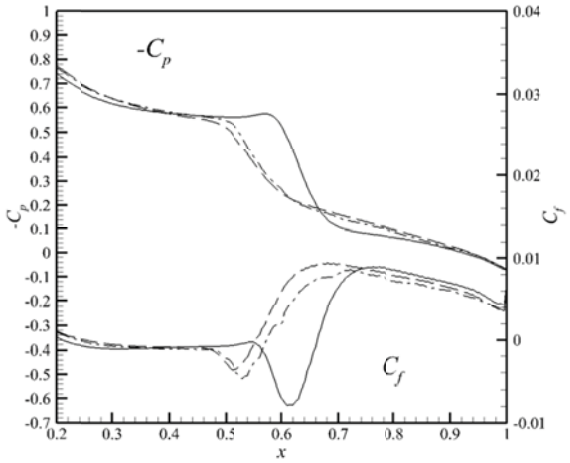

Figure 15. Mean pressure coefficient and mean skin friction coefficient on the wing surface; AoA_4 (solid line, ----), AoA_4c (dash line, - - -) and AoA_4c.n (dash-dot line, -.-.-)

Table 5. Mean lift coefficient, drag coefficient (per unit span) and lift-to-drag ratio

Case	C_L	C_D	C_{Dp}	C_{Df}	L/D
AoA_4	0.600	2.34e-2	1.38e-2	0.97e-2	25.6
AoA_4c	0.593	2.05e-2	1.00e-2	1.05e-2	28.9
AoA_4c.n	0.593	2.09e-2	1.07e-2	1.02e-2	28.4

The mean pressure coefficient and friction coefficient distributions of the cases AoA_4c and AoA_4c.n are shown in Figure 15, in comparison with those of the basic model AoA_4. Both plots of case AoA_4c.n are found very close to those of AoA_4c. The similar behaviors of the mean pressure and friction on the wall in both controlled cases result in similar aerodynamic performances, as listed in Table 5. As shown in Figure 15, the flow separates nearly at the same location in both cases, and the LSB in AoA_4c is smaller than in AoA_4c.n. The minor differences of the plots between the current two cases are associated with the three dimensional instability in the detached shear layer and also possibly the elliptical instability of the shedding vortices. After separation, the K-H

instability takes the dominant role of disturbance growth and the most unstable mode of K-H instability is two dimensional. The three dimensional instability of K-H instability and the elliptical instability of the shedding vortices are still not clear to the authors, and require further investigation in the future.

Effects of the Angle of Attack (AoA)

By adjusting the incidence of the flow and using the same bump configuration in case AoA_4c, the effects of AoA are tested and investigated here. Two more AoAs, 2 deg and 6 deg, are considered. At different AoA, the boundary thickness δ_E is different, and the effects of the bumps will be different. The thickness δ_E of the boundary layer and the ratio of the bump height H_{EF} to δ_E, with the basic model at different AoAs, are listed in Table 6. Figure 16 shows the instantaneous iso-surfaces and side-views of Q-invariant of cases AoA_2 and AoA_2c, and Figure 17 shows those of cases AoA_6 and AoA_6c. The mean pressure coefficient and friction coefficient distributions on the suction surface are shown in Figure 18 for both AoAs. The same results of cases AoA_4 and AoA_4c can be found Figure 10 and Figure 11. The LSBs are diminished in cases AoA_2c and avoided in case AoA_6c as shown by the friction coefficient plots in Figure 18. With the roughness bumps, the recovery of the pressure on the wall for all the controlled cases is much smoother than in the basic models.

Table 6. Parameters of the roughness bumps

Case	X_E	W_{AC}	L_{BD}	H_{EF}	N_{bump}	δ_E
AoA_2c	0.05	0.045	0.045	0.0035	2	0.0046
AoA_4c	0.05	0.045	0.045	0.0035	2	0.0049
AoA_6c	0.05	0.045	0.045	0.0035	2	0.0056

In case AoA_2c, the shedding vortices are found to be disturbed in a similar pattern as in case AoA_4c. In case AoA_6c, the periodic vortical packets are generated behind the bumps in same pattern as in cases AoA_4c.h and AoA_4c.w. With the increase of AoA, the boundary layer thickness δ_E at the bump location $X_E = 0.05$ increases (Table 6), thus the ratio H_{EF}/δ_E decreases. It has been shown previously that at AoA 4 deg and the same location, taller bumps with higher H_{EF}/δ_E ratio in case AoA_4c.h may generate larger disturbances and the vortical packets. However, here the situation is opposite and the vortical packets are generated behind the bumps in case AoA_6c with lower H_{EF}/δ_E ratio. This shows that the effects of the roughness bumps on the flow field are not uniquely determined by the H_{EF}/δ_E ratio, but also by the instability features of the flow field near the location of bumps. Figure 19 shows the mean tangential velocity profiles for the three AoAs at location $X_E = 0.05$. In case AoA_6 the location $X_E = 0.05$ is close to the mean separation point $x = 0.10$ (Figure 18) and the mean tangential velocity profile (Figure 19) is tend to generate the inflection point and separation. In cases AoA_2 and AoA_4, the bumps locate further upstream from the mean separation points. The K-H (inviscid) instability is usually more unstable/has a higher growth rate than the instability in attached boundary layer (Tollmien-Schlitchting instability), thus the profile in case AoA_6 is easier to be perturbed by the bump and causes the generation of the vortical packets.

In current cases, the roughness bumps are more effective on performance improvement at higher AoAs. Table 7 lists the mean lift coefficient, drag coefficient and lift-to-drag ratio for both basic and controlled cases at different AoAs. Figure 20 plots the pressure drag coefficient distributions and the lift-to-drag ratio for all the basic and controlled cases at three AoAs. In the basic cases, the lift and drag are both increasing with the increase of the AoA (Table 7). However, the pressure drag force increases dramatically by more than 50% as the LSB moves upstream with the increase of AoA (Table 7 and Figure 20.b), which causes the deficit of the lift-to-drag ratio at AoA=6 deg (Table 7 and Figure 20.a). In the controlled cases, the lift, the drag and the pressure drag decreases at all the AoAs, though the friction drag slightly increases as with larger turbulent boundary layer flow. The aerodynamic performances are improved in the controlled cases and the benefits of the lift-to-drag ratio gained at each of the AoAs are listed in Table 7 and shown in Figure 20. Especially for case AoA_6c, the lift-to-drag ratio performance has been largely improved comparing with case AoA_6 (Figure 20.a).

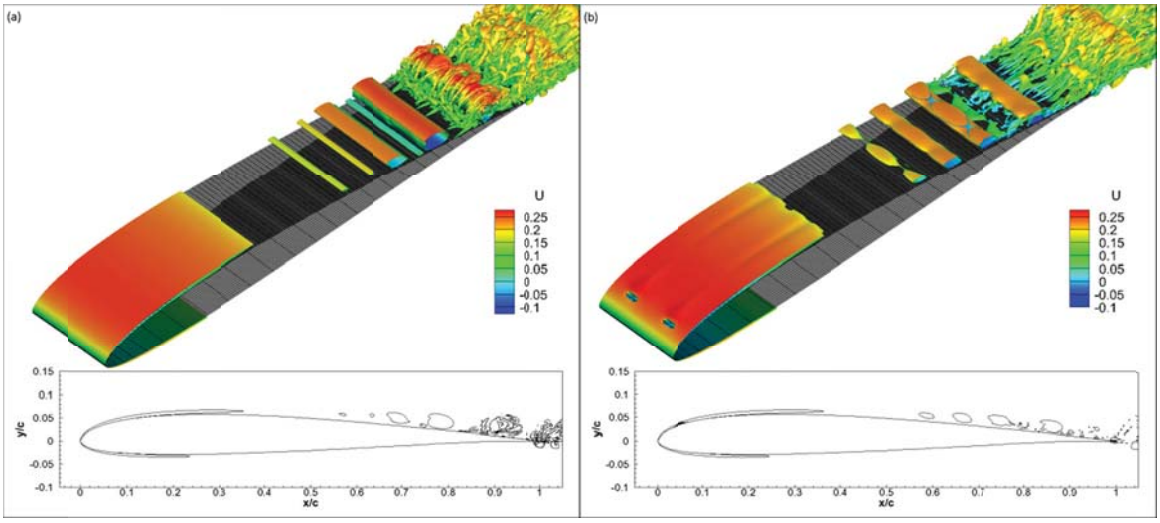

Figure 16. Iso-surface of $Q = 1$ colored by streamwise velocity at $AoA = 2deg$; (a) AoA-2; (b) AoA-2c.

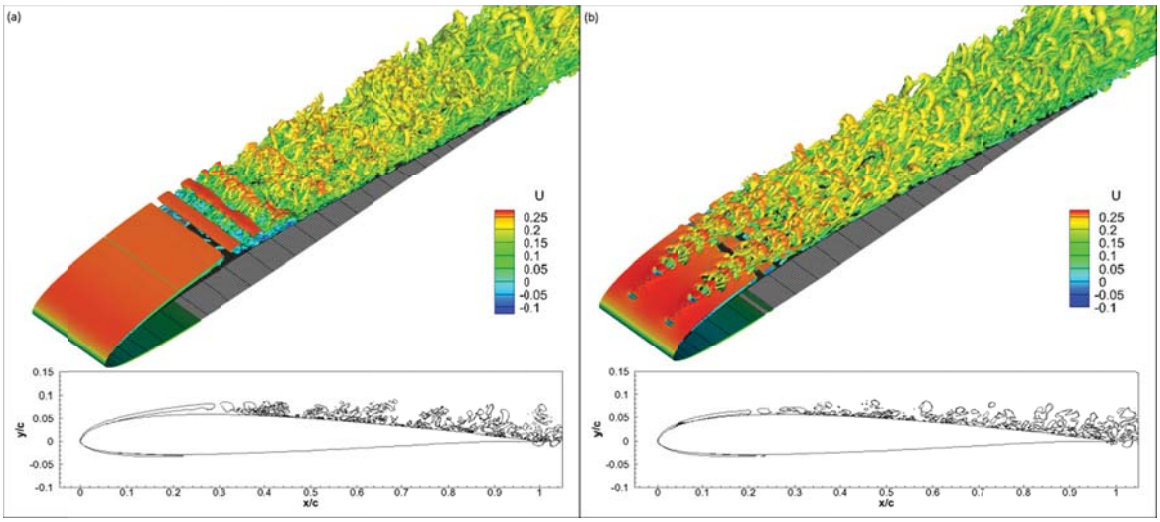

Figure 17. Iso-surface of $Q = 1$ colored by streamwise velocity at $AoA = 6deg$; (a) AoA_6; (b) AoA_6c.

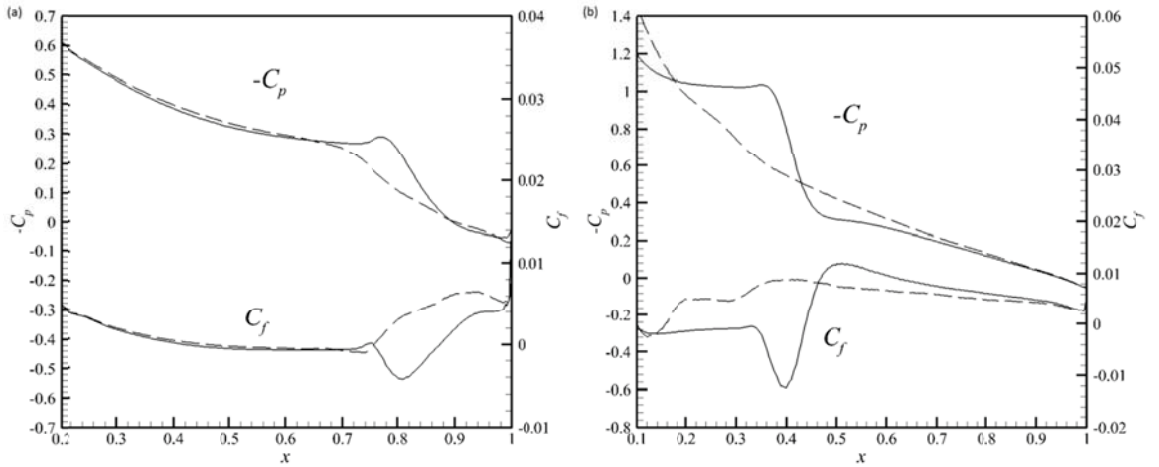

Figure 18. Mean pressure coefficient and mean skin friction coefficient on the wing surface; basic model (solid line, ----) and controlled case (dash line, - - -); (a) $AoA = 2deg$, (b) $AoA = 6deg$

Table 7. Mean lift coefficient, drag coefficient (per unit span) and lift-to-drag ratio

Case	C_L	C_D	C_{Dp}	C_{Df}	L/D	Benefit
AoA-2	0.401	1.68e-2	0.78-2	0.90e-2	23.8	N/A
AoA-4	0.600	2.34e-2	1.38e-2	0.97e-2	25.6	N/A
AoA-6	0.786	3.14e-2	2.15e-2	0.99e-2	25.1	N/A
AoA-2c	0.400	1.63e-2	0.68e-2	0.95e-2	24.5	3%
AoA-4c	0.593	2.05e-2	1.00e-2	1.05e-2	28.9	13%
AoA-6c	0.766	2.56e-2	1.37e-2	1.19e-2	29.9	19%

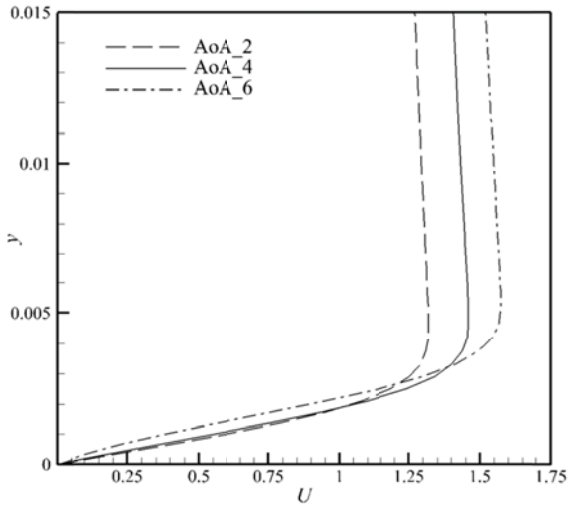

Figure 19. Tangential velocity profiles at $X_E = 0.05$

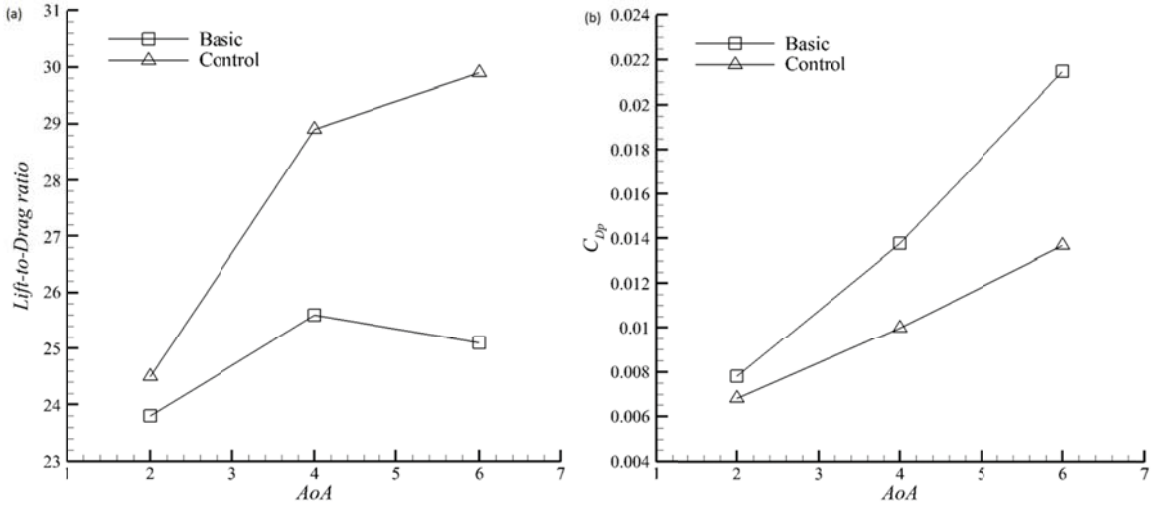

Figure 20. (a) Lift-to-drag ratio and (b) pressure drag coefficient distributions at different AoAs

V. Conclusion

The numerical simulations of a passive flow control technique using roughness bumps on a low-Reynolds number wing are presented in this paper. A high-order spectral difference Navier-Stokes solver is used in the simulations. The numerical results of the basic cases and controlled cases are extensively investigated and discussed.

By introducing the roughness bumps near the leading edge, the LSBs are diminished or avoided depending on the bump geometric parameters. It is found that larger and taller bumps generate larger disturbances, which trigger the vortex breakdown, and delay or avoid flow separation. In addition, the flow also transitions into turbulent flow sooner. Although the friction drag increases slightly, the pressure drag is significantly reduced resulting in an overall drag reduction. The diminishing of LSBs by roughness bumps also slightly reduces the lift. However, the lift-to-drag ratio is significantly increased in the controlled cases. It is also found that no significant change was observed by doubling the number of bumps, but the detailed mechanism requires further study. With a fixed configuration of bumps, the effects of bumps are tested over three AoAs. In the basic cases, the LSB causes a dramatic increase of the pressure drag which may decrease the lift-to-drag ratio with the increase of AoA. In the controlled cases, the aerodynamic performance has been largely improved with the diminishing of the LSB especially at higher AoAs.

Acknowledge

The authors would like to acknowledge the support from the Air Force Office of Scientific Research and the Department of Aerospace Engineering, Iowa State University.

References

[1]Patera, A.T., A Spectral element method for fluid dynamics: Laminar flow in a channel expansion, J. Comput. Phys. 54, 468(1984).

[2]Kopriva, D.A. and Kolias, J.H., A conservative staggered –grid Chebyshev multidomain method for compressible flows, J. Comput. Phys. 125, 244(1996).

[3]D.A. Kopriva, J.H. Kolias, A Staggered-Grid Multidomain Spectral Mthod for the Compressible Navier-Stokes Equations,J. Comput. Phys. 143 (1998) 125-158.

[4]Barth, T.J. and Frederickson, P.O., High-Order Solution of the Euler Equations on Unstructured Grids using Quadratic Reconstruction, AIAA Paper No. 90-0013(1990).

[5]Hu, C. and Shu, C.-W., Weighted essentially non-oscillatory schemes on triangular meshes, J. Comput. Phys. 150, 97 (1999).

[6]Cockburn, B. and Shu, C.-W., TVB Runge-Kutta local projection discontinuous Galerkin finite element method for conservation laws II: General framework, Math. Comput. 52,411(1989).

[7]Abgrall, R. and Roe, P.L., High Order Fluctuation Schemes on Triangular Meshes, Journal of Scientific Computing, Volume 19, pp. 3 – 36, 2003.

[8]Wang, Z.J. and Liu, Yen, Spectral (Finite) Volume Method for Conservation Laws on Unstructured Grids III: Extension to One-Dimensional Systems, J. Scientific Computing, Vol. 20 No. 1, pp.137-157 (2004).

[9]Liu, Y., Vinokur, M., and Wang, Z.J., Discontinuous Spectral Difference Method for Conservation Laws on Unstructured Grids, in Proceeding of the 3rd International Conference in CFD, Toronto, Canada July 2004.

[10]Liu, Yen, Vinokur, M., and Wang, Z.J., Multi-Dimensional Spectral Difference Method for Unstructured Grids, AIAA-2005-0320.

[11]Wang, Z. J., and Liu, Yen, The Spectral Difference Method for the 2D Euler Equations on Unstructured Grids, AIAA-2005-5112.

[12]Huang, P.G., Wang, Z.J., and Liu, Yen, An Implicit Space-Time Spectral Difference Method for Discontinuity Capturing Using Adaptive Polynomials, AIAA-2005-5255.

[13]Y. Sun, Z.J. Wang, Y. Liu, High-Order Multidomain Spectral Difference Method for the Navier-Stokes Equations on Unstructured Hexahedral Grids, Communications in Computational Physics, Vol. 2, No. 2(2007) 310-333.

[14]Y. Zhou and Z.J. Wang, "Implicit Large Eddy Simulation of Transitional Flow over a SD7003 Wing Using High-order Spectral Difference Method", AIAA-2010-4442.

[15]P. L. Roe, Approximate Riemann solvers, parameter vectors, and difference schemes, J. Comput. Phys. 43 (1981) 357-372.

[16]Galbraith, M. and Visbal, M., Implicit Large Eddy Simulation of low Reynolds number flow past the SD7003 airfoil," Proc. of the 46th AIAA Aerospace Sciences Meeting and Exhibit, Reno, Nevada, AIAA-2008-225, 2008.

[17]Zhou, Y. & Wang, Z. J. 2010 Absorbing Boundary Conditions for the Euler and Navier-Stokes Equations with the Spectral Difference Method, Journal of Computational Physics 229, 8733-8749

[18]Volino, R. J., and Hultgren, L. S., 2001, Measurements in Separated and Transitional Boundary Layers Under Low-Pressure Turbine Airfoil Conditions, ASME J. Turbomach., 123, pp. 189–197.

[19]Ol, M. V., Hanff, E., McAuliffe, B., Scholz, U., and Kaehler, C., 2005, "Comparison of Laminar Separation Bubble Measurements on a Low Reynolds Number Airfoil in Three Facilities," 35th AIAA Fluid Dynamics Conference and Exhibit, Toronto, Ontario, June 6–9, AIAA Paper 2005-5149.

[20]Burgmann, S., Brucker, S., Schroder, W., 2006, Scanning PIV Measurements of a Laminar Separation Bubble, Exp. Fluids, 41, pp. 319 – 326.
[21]Hu, H., Yang, Z.F., An Experimental Study of the Laminar Flow Separation on a Low-Reynolds-Number Airfoil, MAY 2008, Vol. 130 / 051101-1
[22]Spalart, P. R. & Strelets, M. K. H. 2000 Mechanisms of transition and heat transfer in a separation bubble. J. Fluid Mech. 403, 329–349.
[23]Jones, L. E., Sandberg, R. S. & Sandham, N. D 2008 Direct numerical simulations of forced and unforced separation bubbles on an airfoil at incidence. J. Fluid Mech. 602, 175–207.
[24]Saric WS, Carrillo Jr. RB, Reibert MS, 1998. Leading-edge Roughness as a Transition Control Mechanism, AIAA Paper Number 98-0781
[25]Saric WS, Reed HL 2002. Supersonic Laminar Flow Control on Swept Wings Using Distributed Roughness, AIAA Paper Number 2002-0147
[26]White, E.B., & Saric, W.S., Application of variable leading-edge roughness for transition control on swept wings, AIAA paper 2000-0283.
[27]R. Honsaker* and W.W. Huebsch, 2005, Parametric Study of Dynamic Surface Roughness as a Mechanism for Flow Control, AIAA 2005-4732
[28]Fransson, J. H. M., Talamelli, A., Brandt L. & Cossu, C. 2006 Delaying transition to turbulence by a passive mechanism. Phys. Rev. Lett., 96, 064501.
[29]Fransson, J. H. M., Brandt L., Talamelli, A. & Cossu, C. 2005 Experimental and theoretical study of the stabilization of Tollmien-Schlichting waves by finite amplitude streaks. Phys. Fluids, 17, 054110.
[30]Dubeif, Y. and Delcayre, F., “On Coherent-vortex Identification in Turbulence,” Journal of Turbulence, Vol. 1, No. 11, 2000, pp. 1-22.